Monitoring structural scale composite specimens in a post-buckling regime: The integrated finite element stereo digital image correlation approach with geometrically non-linear regularization

John-Eric Dufour, G. Colantonio, Christophe Bouvet, Jean-Noël Périé, Jean-Charles Passieux, Joël Serra

Monitoring structural scale composite specimens in post-buckling regime: the Integrated Finite-Element Stereo Digital Image Correlation approach with geometrically non-linear regularization

J. -E. Dufour[1,*], G. Colantonio[1], C. Bouvet[1], J. -N. Périé[1], J. -C. Passieux[1] and J. Serra[1]

[1]Université de Toulouse, Institut Clément Ader, ISAE-SUPAERO – UPS – IMT Mines Albi – INSA Toulouse, FRANCE

**corresponding author: jdufour@isae-supaero.fr*

Abstract

Background: Even though the simulations used to describe the failure of laminates are becoming more and more predictive, complex testing under multiaxial loadings is still required to validate the design of structural parts in a wide range of industrial domains. It is thus essential to assess the actual boundary conditions to allow for an objective comparison between testing and calculations, in particular since the structural tests are complex and often leads to buckling. Therefore, accurate estimation of force and moment fluxes applied to the specimen is critical. In this context, stereo DIC has proven to be an important measurement tool and provides very well resolved surface displacement fields, but the exploitation of such measurements to calculate fluxes remains problematic when testing composites. **Objectives:** The first objective of this study is both to reduce the uncertainty associated with fluxes determination on a complex test and to simplify the extraction process with respect to existing procedures. The second objective is to make this methodology robust to geometrically nonlinear deformations. **Methods:** In this paper, we propose a new methodology that extracts minimal boundary conditions in the form of 3D mechanically admissible displacements fields. The approach developed uses a Finite-Element Stereo Digital Image Correlation (FE-SDIC) method regularized by the means of mechanical behavior admissibility equations. **Results:** Results show that the new methodology outputs much more accurate fluxes than classical data generated from multiple differentiations of the displacement fields. Excellent noise robustness is obtained and quantified. **Conclusions:** Numerical predictions have been satisfactorily compared with experimental data from one structural scale composite specimen under complex testing.

Keywords: Digital image correlation; Mechanical regularization; Post-buckling; Composite structures; Boundary Conditions

Introduction

Composite structures are now largely used in most transport vehicles, especially in the aerospace and astronautics fields [1]. In practice, the development and certification of these structures are still based on experimental validations in an approach known as the "test pyramid" initially developed by Rouchon et al. [2]. The concept was also used in other domains such as the automotive engineering [3]. Tests are performed on coupons under uniaxial loading. The upper levels of the pyramid are validated using much more complex tests on specimens that are increasingly closer in shape and size to the final design of the different parts. The complexity of these tests leads to two major issues.

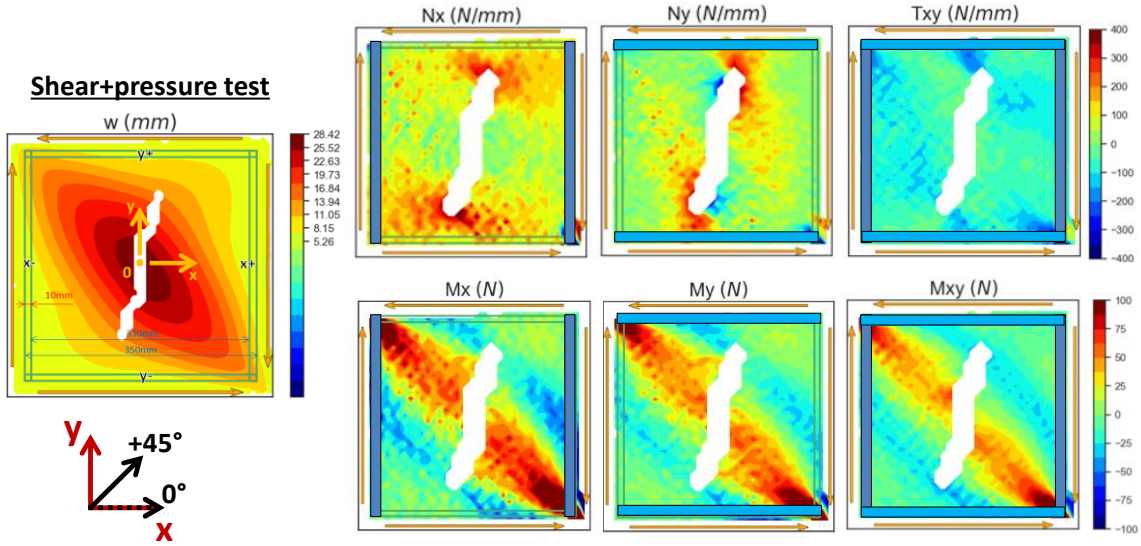

Figure 1: Forces and Moments fluxes distribution for a shear+pressure test on a notched composite plate just before total failure – the rectangular arrays are the averaging zones used to output scalar values [4]. This test has been perform using a similar set-up as the one describe later in section 2.2

First, unlike uniaxial coupon testing, it is most of the time impossible to accurately know what load is really going through the specimen given the displacement of the far acting actuators. Recent research [4] exhibits the fact that the force and moment flux distributions are very far from being homogeneous in space (Figure 1) or time. It is, however, necessary to describe accurately the repartition of the load fluxes in the specimen throughout testing and up to failure in order to output limit and ultimate forces and moments fluxes to help the design process [1].

The maximum load that an aircraft is expected to undergo at any point in the service life is referred to as the limit load [5]. Limit loads can be expected in any given direction (forward or down, etc.) or a combination of more than one direction. Under limit load conditions, the Federal Aviation Administration regulations require that the aircraft components support those loads without any permanent detrimental deformations and that the stresses remain below the critical yield point. Although the aircraft is not expected to be subjected to loads above the limit loads, there is a need for an additional safety factor to account for unexpected events such as a sudden and severe gust load in a storm on a wing for example, or an emergency landing or crash condition. Such loads are defined as ultimate loads and a classical safety factor applied to limit loads is 1.5. The use of fluxes is relevant since, in the classical laminate theory, the forces and moments fluxes (respectively in N/mm and N)

are related to the strain and curvature with the ABD matrix [1]. These fluxes represent the load and moments taken by the plate per unit length.

Regarding the fluxes determination, Grotto et al. [4] exploited the surface displacements obtained from stereo DIC (S-DIC) and used the Classical Laminate Theory (Figure 2) to compute the moment and force fluxes from the top surface observation. This methodology was only valid for zones where there is no damage and was relatively time consuming. This methodology had additional limitations due to the number of differentiations needed: 1 differentiation for the planar displacement to obtain the strains and 1 for the out of plane displacement to obtain the curvatures which makes it highly sensitive to noise. Indeed, deriving a noisy set of data can lead to incorrect estimation of the quantities of interest (here the applied forces and moments fluxes). **The first objective of the research presented in the current paper is to develop and implement a methodology that helps both reducing the uncertainty associated with fluxes determination on a complex test and simplifying the extraction process.**

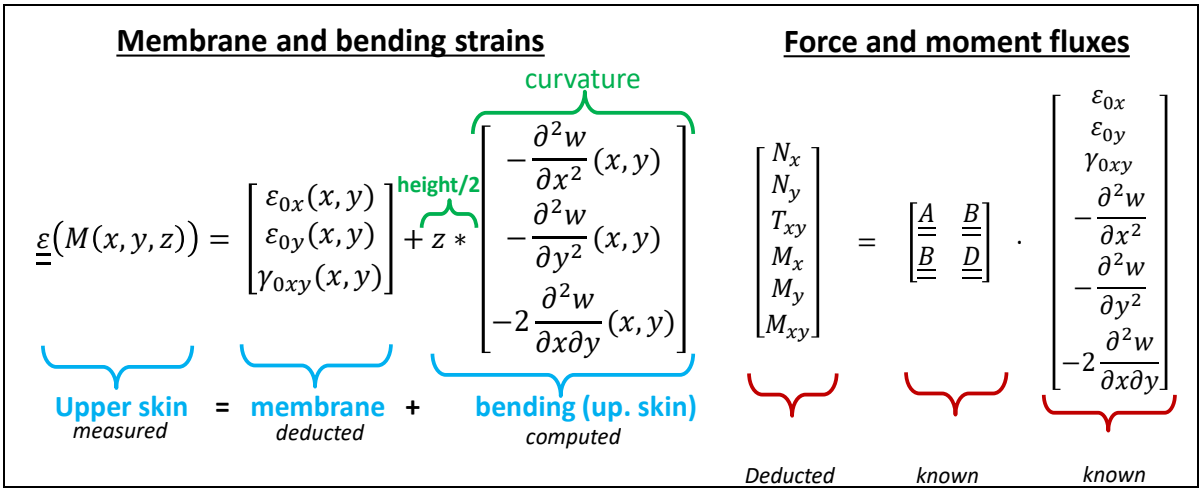

Figure 2: Obtaining the force and moment fluxes from the upper surface displacement using classical laminate theory [4]

Second, as detailed by Serra et al. in the research associated with the VERTEX project ([6], [7]), even though the experimental approach is very robust, it is extremely costly. Indeed, with this certification method, thousands of tests are necessary to validate the integration of a new material/design in an aircraft. Research has therefore focused on the development of numerical models that simulate the behavior of the composite structures up to failure. A tremendous amount of work has been done at the coupon level [8]–[15] but only a few teams tackle the challenge of modeling the behavior of composite structures at the technological scale with a high degree of fidelity [16], [17].

In such complex multiaxial tests, the influence of boundary conditions goes beyond the linear superposition of its uniaxial components [18]–[23]. When validating a numerical model, the actual experimental boundary conditions must be applied with great care in the model. The complexity of numerical simulation at this scale comes mainly from the difficulty to assess accurately the exact boundary conditions of a structural scale specimen under multiaxial loadings.

The redundancy of the loading paths and the several stress concentrations (notches, bolted joints…) make it necessary to have an *in situ* monitoring of the tests to know which loads and displacements are really applied to the specimen. The emergence of stereo Digital Image Correlation (DIC) methods helped a lot on these issues with 3D displacements that can now be measured on the surface of the specimens through time. DIC consists in calculating a displacement field from digital images of the specimen taken before and after loading. The limited amount of information (1 scalar value per pixel), its quantization (1 integer between 0 and 255) and its discrete repartition (sampling), makes DIC an ill-posed problem. Several approaches to circumvent this issue have been employed. The most common one is to assume the unknown displacement to be continuous over the entire Region of Interest. It is usually sought as a linear combination of a set of shape functions that can be of different types [24]–[26]. One convenient choice is offered by meshes used in the Finite Element (FE) Method because it allows for straightforward connections between experiment and simulation: the same FE mesh used for the displacement field measurement can also be used for numerical analyses [27], [28]. This approach was named “Global” by opposition to the “Local” ones that consider disconnected subsets independently [29].

Regarding the boundary conditions extraction and use in numerical models, one convenient methodology is to exploit surface displacement fields measured by S-DIC around the area of interest and derive Dirichlet boundary conditions to be applied to the FE model [30]. This methodology has proven its efficiency [7], [16], [17], [22], [31], [32] but shrinks a lot the zone of interest if one wants to be sure that the plate bending behavior is well described. Indeed, in 2D cases, only one node layer is sufficient but several layers are required in 3D, thus.

Another solution when using shell elements can be to apply the displacement in the 3 directions as well as the rotations for a single node layer [34]. To obtain the rotations, one differentiation of the displacement field is, however, needed and increases uncertainty. Moreover, volume elements are sometimes mandatory in FE models when the degree of complexity goes beyond the limitations of shell elements. Even if techniques connecting shell and volume elements exist, the easiest solution is still to keep the same type of element in the region where the boundary conditions are applied and in the area of interest. In the following, we will therefore place ourselves in this configuration and use volume elements. In that case, as illustrated on Figure 3, the displacement of both the lower and upper surface should be imposed to represent correctly the rotations while still using only one “row” of nodes. However, as often during structural testing, the optical access is here limited and only one side of the panel can be instrumented. The displacements on the opposite side cannot consequently be measured. The resulting increase in the number of unknown therefore calls for an extra regularization of the problem. One idea may be to assist image correlation using mechanics [35], i.e., to look for displacements that allow for good image registration while being mechanically admissible. We will subsequently rely on the knowledge of the laminate behavior (here supposedly remaining elastic) in a restricted region that could be considered as a "spring element".

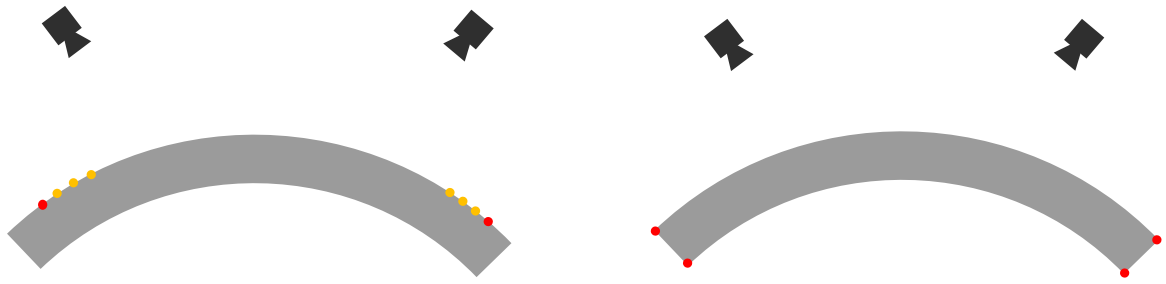

Figure 3: Existing (left) vs. proposed (right) extraction procedure to apply boundary conditions to the simulation.
On red nodes both in-plane and out of plane translations are applied.
Only out of plane translation are enforced for orange nodes.

The major advantage of the global approach to DIC, used hereafter, is that one can precisely inject in the formulation the expected regularity of the displacement field from the beginning (e.g., a more or less strong constraint on the search space)[35]–[45], rather than projecting it *a posteriori* on a reduced basis (e.g., to obtain smooth derivatives). This kind of approach allows to limit the influence of image noise on the displacement measurement or even the identification of constituent parameters [46]. Two main approaches can be distinguished. The first, referred to as regularized DIC, is to use a weak regularization. In practice, a mechanical regularization term (e.g., based on the deviation from equilibrium) is added to the correlation functional [41], [45]–[47]. The second one, referred to as integrated DIC, consists in using as trial field a displacement field solution of a mechanical problem. A generalization based on the exploitation of test displacement fields from FE simulation was later proposed by Leclerc et al. [48]. This type of approach has been widely exploited on many problems [40]–[44], [47], [49]. Pierré et al. [28] took advantage of this approach to extract displacement and use them as boundary conditions. To the knowledge of the authors, this last reference reports the most advanced piece of research on such subject. However, the methodology presented was developed and tested for a plate undergoing linear elastic bending. Improvements to the classical use of mechanical and Tikhonov regularization method have thus been developed to extend the domain of application to specimen undergoing highly non-linear deformation such as the ones tested using the multiaxial VERTEX test rig [6], [7]. **The second objective of the research presented in the current paper is to develop and implement a methodology to extract boundary conditions in the form of 3D displacements on a single pair of rows of nodes (top and bottom surface) for large composite panels undergoing geometrically non-linear deformation.**

1. Regularization method

1.1. Image correlation

In this work, as 3D displacement measurements were needed, a 3D surface Digital Image Correlation (stereo-DIC) method has been used. Recent developments on global approach to stereo-DIC have shown the great adaptability and resilience of the method. Moreover, the FE-SDIC method simplifies the comparison between experimental results and numerical simulation by using finite element shape functions as a basis in the measurement algorithm.

The FE-SDIC formulation used in this paper can be derived from the minimization of the gray level residual between a reference picture I_{ref} and a deformed picture I_{def}:

$$u = argmin \sum_{cam} \int_{\Omega} (I_{ref}(S, cam) - I_{def}(u, S, cam))^2 \quad \text{Eq. (1)}$$

With, as described in previous work [24], [28], [45], u, the unknown 3D displacement, *S* the model of the observed surface (usually a mesh) and *cam* the projector relating the 3D world coordinates to the 2D pixels of the image. In order to solve this problem in a finite dimension space, displacement *u* is chosen to depend on a finite number of parameters **q**, sometimes referred to as degrees of freedom. A Gauss-Newton scheme is used to minimize the above minimization problem. At iteration k, the linearization around the solution u written as a function of parameters **q** [28] leads to :

$$\left(\sum_{cam} \mathbf{M}_{dic}^{cam,k}\right)\mathbf{q} = (\sum_{cam} \mathbf{b}_{dic}^{cam,k}) \quad \text{Eq. (2)}$$

with $\mathrm{M} = \int_{\Omega} \nabla I_{ref} \frac{\partial u}{\partial q} \times \nabla I_{ref} \frac{\partial u}{\partial q}$,

$b = \int_{\Omega} \nabla I_{ref} \frac{\partial u}{\partial q} \times (I_{ref} - I_{def})$,

And *cam* is the camera's index.

Among the different choices available to describe the displacement u, we chose to use the same finite element basis as the one used in the simulations. The elements in this case are Abaqus' SC8R continuum shell, corresponding to an 8-node hexahedral element with the associated kinematic basis (3 translations per node).

This choice of basis for the displacement field allows for a strong coupling between the DIC measurement and the simulations. This link can be useful to compare results but can also be taken advantage of to improve the measurement process by adding some form of regularization.

1.2. Mechanical regularization

The DIC problem mentioned previously is ill-posed, and thus needs regularization. As already described in the literature, several techniques can be used to regularize the problem. These choices can be separated into two categories. First, the penalization methods, which will be referred to as weak regularization, consist in penalizing the solution so that it satisfies at best certain properties. The strong regularization, in which the solution space is directly constructed to satisfy the required properties, constitutes the second category. This type of regularization applied to DIC is often denotes as "integrated" [36], [42], [44], [47], [50]–[52]. Any prior information regarding the sought quantity can be used to improve the convergence of the algorithm and find a solution. In this particular case, the displacement of interest must satisfy some basic properties guaranteed by the mechanical principles.

Remark. The use, as a regularization technique, of the finite element (or subset) size, within which the displacement is restricted to follow a low degree polynomial evolution, falls into this second category of strong regularization.

As the sought displacement solution is the image of the mechanical state occurring in the sample, it must also satisfy the equilibrium equation. The DIC problem is written in a Finite Element sense. This equilibrium constraint writes in a classic finite element framework:

$$\mathbf{K}\mathrm{q} = \mathrm{F} \qquad \text{Eq. (3)}$$

This expression can be subsequently divided between interior and boundary nodes (Figure 4).

The previous equation thus reads:

$$\begin{pmatrix} K_{ii} & K_{ib} \\ K_{bi} & K_{bb} \end{pmatrix} \begin{pmatrix} q_i \\ q_b \end{pmatrix} = \begin{pmatrix} 0 \\ F_b \end{pmatrix} \qquad \text{Eq. (4)}$$

The first line of this equation links the displacement of the interior nodes to the boundary nodes and can be rewritten as:

$$q_i = -K_{ii}^{-1} K_{ib} q_b \qquad \text{Eq. (5)}$$

The entire displacement field q can therefore be expressed completely as a function of the boundary displacement and the stiffness K [28]:

$$q = \begin{pmatrix} -K_{ii}^{-1} K_{ib} \\ I_{bb} \end{pmatrix} q_b = L\, q_b \qquad \text{Eq. (6)}$$

In this work, we chose to construct the solution space from the mechanical model of the plate, hence describing the displacement of the whole sample as a function of the stiffness and its boundaries solely. The first reason is the presence of an hourglass while solving this problem using a weak mechanical regularization. Moreover, the knowledge of the material model is assumed reliable in this case, and the boundary conditions and load are searched for. This regularization provides a better resilience to noise by acting as a mechanical filter.

Remark. The inversion of the operator K_{ii} is costly and should not be performed directly. Given the ratio between the number of interior and boundary unknowns, the product $K_{ii}^{-1} K_{ib}$ can be directly computed using an efficient solver with multiple right-hand sides.

In this work, the specimen is actually considered as a test body to measure force fluxes. It relies on an estimation of the stiffness that is assumed trustworthy. During the tests, the center of the sample is experiencing inelastic phenomenon (damage, failure…) and our model is not accurate enough. This zone was removed from the analysis as illustrated in Figure 4. In Pierré et al. [28], a linear elastic model was used but is insufficient to process the geometric non-linearity due to buckling in our tests as will

be shown later. By doing so, the new set of (interior) boundary node has to be added to q_b, as illustrated on Figure 4.

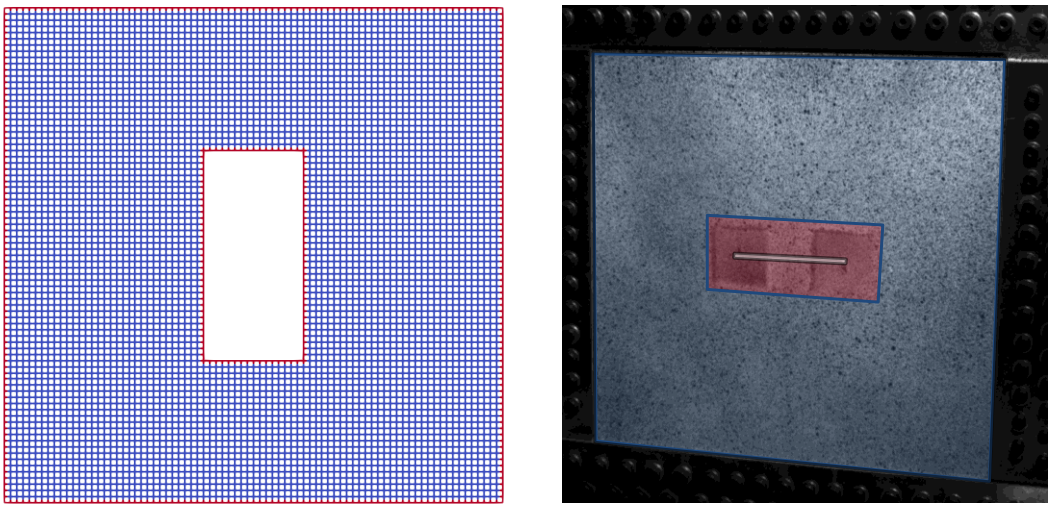

Figure 4 : (left) Separation between interior (blue) and boundary (red) nodes on the plate model. (right) Picture of the observed plate. The red part is masked and not taken into account in the DIC to avoid non-linear perturbation from the cracks propagation. The boundary between the blue and red zone is a boundary condition and thus an unknown to be determined.

The DIC equation described earlier thus becomes:

$$L^T M_{DIC} L \, q_b = L^T b_{DIC} \qquad \text{Eq. (7)}$$

With q_b the nodal displacement of the boundaries, and L the linear operator defined in Eq. (6).

As already known and described in the literature, this approach is a projection of the problem on a smaller sub-space. This approach thus performs a natural filtering of the problem, and any effect not accounted for will not be properly measured. Nevertheless, it is possible to check the image correlation residuals map to see if this is the case or not and adapt the model.

1.3. Tikhonov regularization

The strong regularization can be used to express the displacement of the bulk of the model as a function of its boundaries, thus greatly limiting the number of degrees of freedom to be estimated. This reduction is not always sufficient to allow the resolution of the DIC problem. The motions of some of the boundary nodes (especially the bottom layer ones) do not influence the top displacement field. The problem is badly conditioned and could even singular. In order to prevent this problem, the boundaries themselves may be regularized to avoid spurious perturbations in the measurement.

Remark. At this point, a parallel can be made with the Saint-Venant's principle. This principle states that far enough from the boundaries, the mechanical state is as if only the resulting forces and moments of the actual load was applied on the boundary. Reciprocally, any distribution of forces and moments with a zero resultant influences the displacement close to the edges only. In other words,

the boundary conditions distribution is not unique. The regularization of such short wavelength effects is a complex task in DIC as it spreads on a small number of elements. As we are only interested in the part of the boundary conditions that has an effect at long wavelength, a particular solution is chosen using Tikhonov regularization on the boundary.

In this work, each node of the boundary is penalized to avoid non-physical behavior. Each edge of the elements belonging to the boundaries is associated with stiffness (like a spring) along each direction, thus penalizing the difference in displacement between two consecutive nodes along the boundary as schematized on Figure 5.

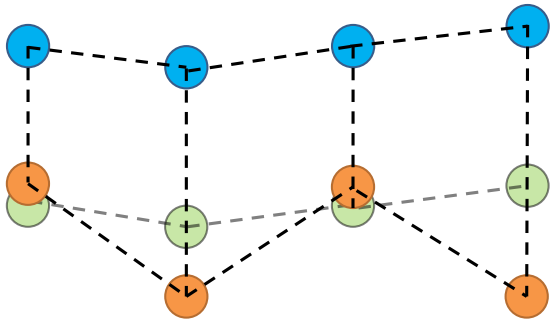

Figure 5 : Illustration of the effect of the penalization of the boundary nodes. Orange nodes tend to behave erratically due to the lack of constraint. By adding stiffness to the connecting edges (dashed lines), their displacement is driven by the other (constrained) degrees of freedom.

For each direction *dir* and each *edge* an elementary penalty operator can be constructed as:

$$T_{edge}^{dir} = \omega_{dir} \begin{pmatrix} 1 & -1 \\ -1 & 1 \end{pmatrix} \quad \text{Eq. (8)}$$

Where ω_{dir} is the weight of the penalization associated with the direction dir. The full penalization operator T is then constructed from the assembly of all the elementary ones.

The measurement problem can be reformulated as follows with a penalization on the displacement U_b :

$$U_b = argmin \sum_{cam} \int_{\Omega} \left(I_{ref}(S, cam) - I_{def}(LU_b, S, cam)\right)^2 + \omega \left|\left|U_b\right|\right|_T^2 \quad \text{Eq. (9)}$$

Where ω denotes a global penalization coefficient.

The associated DIC linear system to be solved thus becomes:

$$(L^T M_{DIC} L + \omega T)\delta q_b = L^T b_{DIC} - \omega T q_b \quad \text{Eq. (10)}$$

It should be noted that penalizing an out-of-plane edge tends to prevent any change in thickness of the model. This is (most of the time) beneficial since no information on the depth of the material is

available from a one-sided observation. Moreover, hourglass or other spurious modes tend to appear even in-plane if the adjacent nodes are not penalized because of occultation issues on the boundary for example. Rigid body motions of the boundary are not penalized by this approach.

The regularization parameter ω can be chosen using standard techniques like L-curves (Figure 6) but a specific care should be given to the different directions to differentiate the penalty between them. More details will be given regarding this differentiation in the following section. In our case, the range of Tikhonov coefficient usable is actually pretty wide (as already pointed out using Saint-Venant's principle), but it is clear that the problem must be regularized to converge. We investigated the impact of a penalization coefficient on the Tikhonov regularization and concluded that not only we had to pick it large enough to avoid singular matrix issues (Tikhonov coefficient < 1, Figure 6) and low enough to avoid non-physical solutions (Tikhonov coefficient > 1000000, Figure 6).

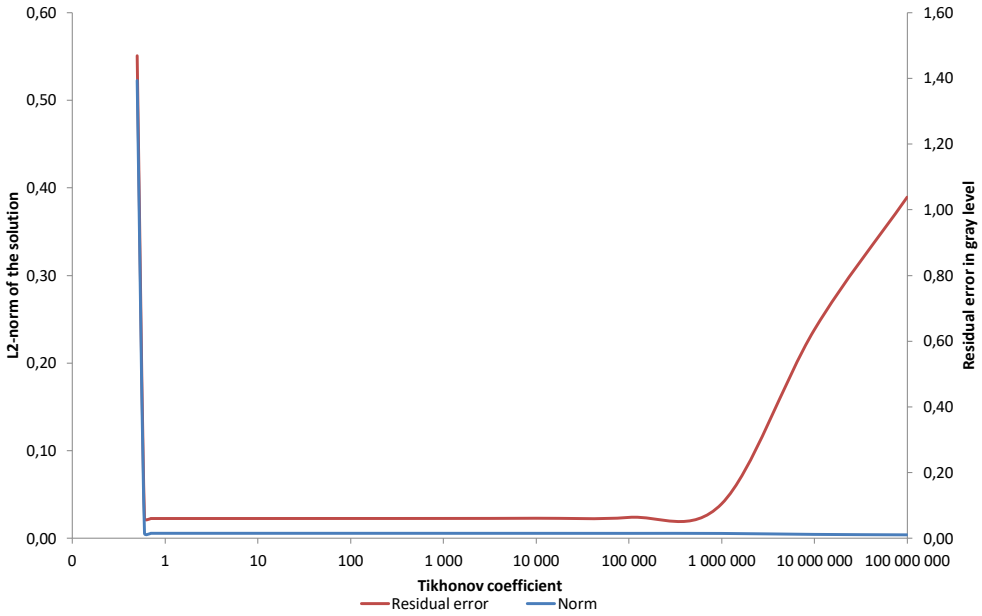

Figure 6: L-curves (Residual error and L2-norm of the solution) corresponding to the flexural case presented in section 3.1. The chosen parameter in this case is 1.

2. Experimental test cases

2.1. Flexural test

We chose to study the same flexural test as the one analyzed by Pierré et al. [28]. A thin plate composed of a layer of PVC surrounded by two layers of Aluminum is clamped in A, while B is moved vertically, thus creating a flexural loading inside the plate. The setup is illustrated in Figure 7. Pictures of the experiment are taken at different displacement amplitudes using 2 AVT Pike cameras with a 2402x2052 sensor. Figure 7 (right) shows an example of the pictures taken.

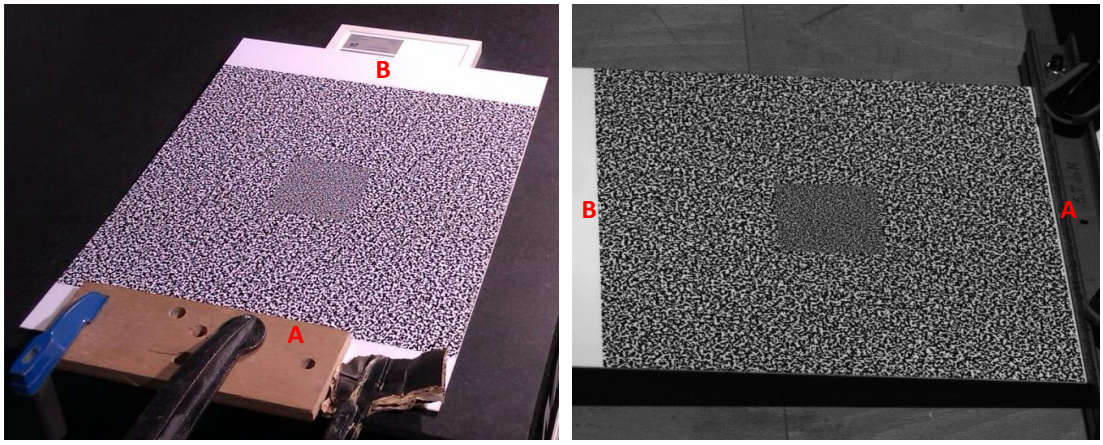

Figure 7 : (left) Experimental setup used to load the plate; (right) Image taken from the left camera of the Stereo-DIC rig

The displacement of the plate is measured from the digital images using 2 different DIC methods, the VIC-3D™ software version 7.2.4 (local approach) and the FE-DIC code Pyxel (global approach) developed at the Institute Clement Ader. Figure 8 shows the displacement fields (u and w) along the longitudinal (X) and out-of plane (Z) directions using the VIC software. The results are consistent with a simple plate subjected to bending. The out-plane displacement is increasing from the right (0mm, the plate is clamped on this side) to the left (5.2mm as the displacement is prescribed on this side of the plate). The magnitude of the longitudinal displacement is about 50 times smaller but presents a similar distribution, as it could be expected. It should be noted that, even if in general for stereo DIC, the uncertainty on the out-of-plane displacement is significantly larger than on in-plane ones [53], in the present case, the signal-to-noise ratio remains largely in favor of the out-of-plane displacement.

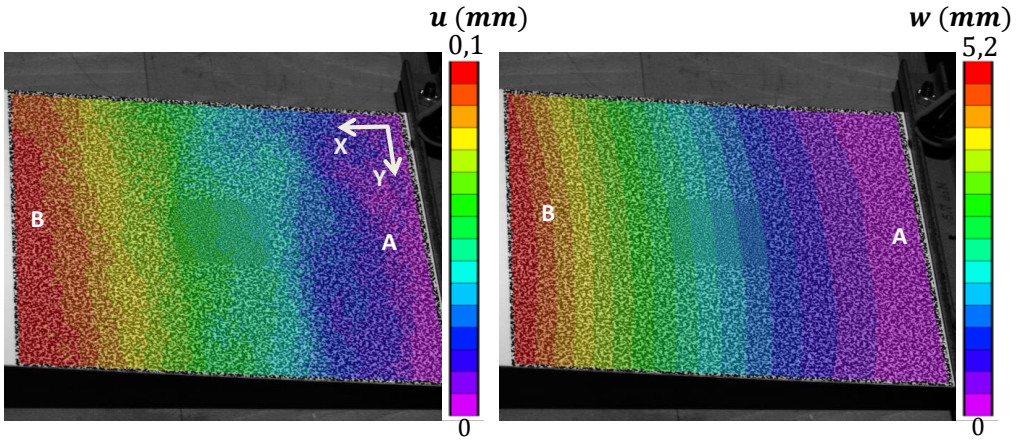

Figure 8 : Displacement fields (in mm) along the X direction (left) and the out of plane direction (right) using the VIC software (with a local approach to DIC). The subset size is 39 pixels and the step size is 13 pixels.

The same experiment and images are processed using the FE-DIC code Pyxel, following the principles described in section 1. The full plate is thus modeled and a 3D Finite Element mesh is used as the support of the measurement. First, a strong regularization of the displacement field is used along with a weak penalization on the edges (using the spring-like Tikhonov regularization, as described in section 1.3) of the same magnitude along all directions (in-plane and out-of-plane). The displacement fields obtained using these parameters are shown in Figure 9. It can be observed that the out-of-plane displacement field seems completely satisfactory and very close to the one obtained using the local approach. However, along the longitudinal direction, the displacement obtained is very different. Even

if, along the middle line of the plate the measurement is close to the real one, its amplitude vanishes to 0 on the top and bottom edges which is actually not the case. We associated this vanishing effect with an overweighted penalization of the edges, preventing the (small) in-plane displacement to be measured correctly.

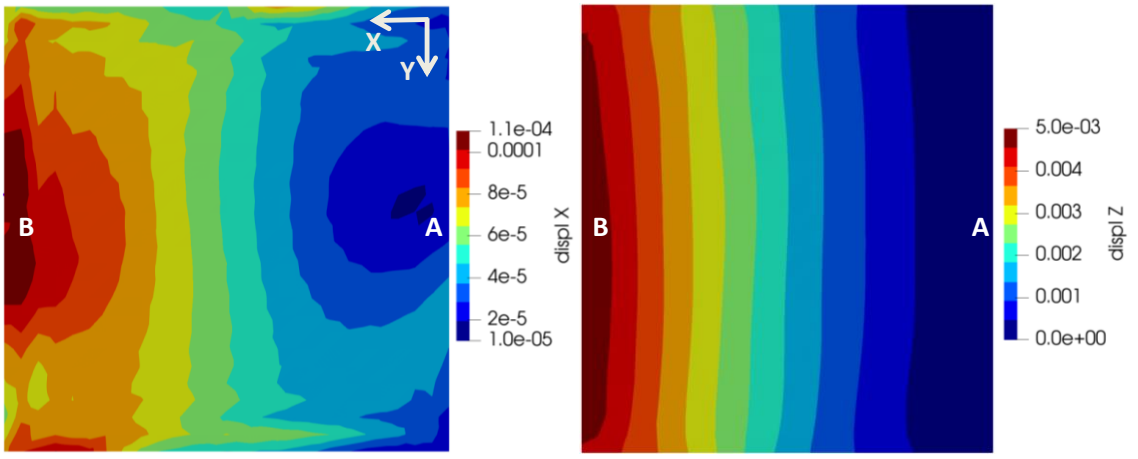

Figure 9 : Displacement fields (in m) along the X direction (left) and Z direction (right) obtained with a strong mechanical regularization and the same Tikhonov penalization along each direction

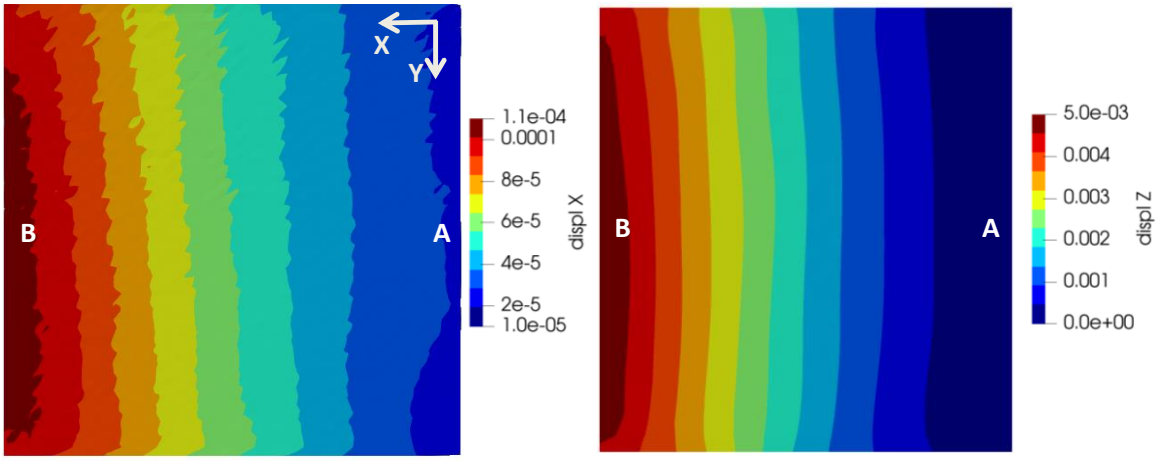

Figure 10 : Displacement fields (in m) along the X direction (left) and the Z direction (right) using a strong mechanical regularization and a differentiated Tikhonov penalization along each direction

One solution to this issue consists in using a different weight along the different directions depending on the stiffness of the problem in the different directions. Figure 10 shows the displacement fields obtained using a strongly regularized DIC method and an adapted Tikhonov penalization along each direction. We can observe that the out-of-plane displacement is still the same as before, which is to be expected. The longitudinal displacement field is significantly improved. By decreasing the weight of the penalization, the signal can now be measured correctly on the boundaries without perturbations. This adapted penalization will thus be used in combination with the strong regularization in the remaining of this paper.

In order to offer a reference displacement field to compare our results to, a simulation of an idealized setup has been performed. The plate is thus modeled on Abaqus™ 2018 and the right edge is clamped while the displacement of the central part of the leftmost line of nodes is imposed in accordance with

the amplitude found using the DIC. Our measurement results are perfectly consistent with the simulated ones.

As explained in the introduction, this work does not only focus on displacement measurement but also on force and moment fluxes estimation. Given the specific loading applied to the plate, the expected fluxes should be an increasing moment about the transverse axis Y ranging from 0 on the left side of the plate (prescribed displacement) to a maximum on the right side (which is clamped).

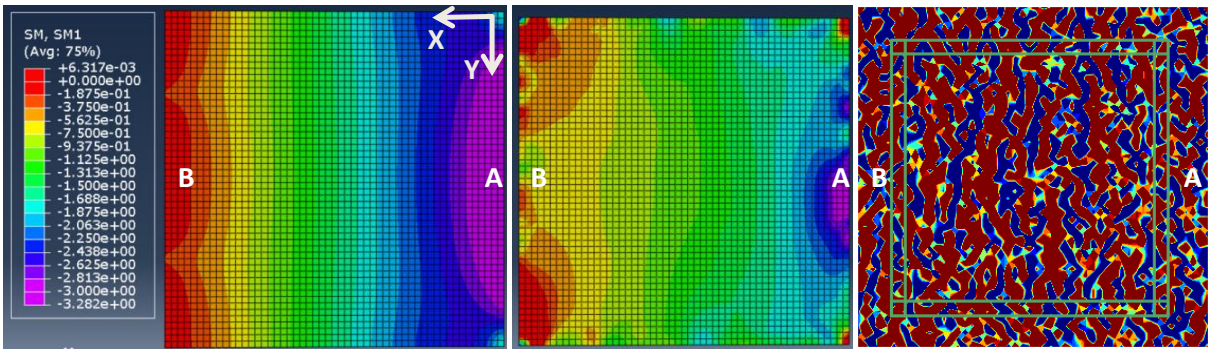

Figure 11: Moment flux (in N) about Y axis as simulated by an Abaqus simulation (left), extracted from strongly regularized DIC measurement (middle) and post-processed from a VIC measurement (right).

The procedure described to estimate the fluxes from a surface measurement [4] can be carried out on this experiment to estimate the real fluxes passing through the sample.

Figure 11 (right) shows the resulting moment field as obtained using derivatives of surface measurement with the classical laminate theory. It can be seen that the very low robustness to noise mentioned above, does not allow estimating, even roughly, the moment field. The displacement fields obtained using VIC in this case are not suitable for this analysis and the resulting moment field does not provide a good estimate of the fluxes.

The strongly regularized method we described in the previous section can also be used to estimate fluxes in a simplified way. As the displacement is measured on all the nodes of the FE model, the complete mechanical state of the sample can be recovered from the corresponding FE simulation with prescribed displacements associated with all the nodes. Therefore, the fluxes are directly estimated from the finite element solution using the forward problem KU = F, without any additional differentiation step involved.

In this work, the finite element solver Abaqus™ is used to conduct this analysis and the fluxes can then be extracted from the solution. The estimated moment filed from the strongly regularized DIC method is shown on

Figure 11 (center). It is worth noting that as opposed to the classical procedure used previously; this method is filtering a large part of the noise by construction as mentioned in the previous section. The proposed method is much more robust to noise and the estimated field is consistent with the sought moment field.

To investigate whether the results from the post-processing approach were caused by a mistake in the method or other factors such as noise, a purely artificial case was produced and processed. A pair of real images was used as a reference and deformed by the displacement field extracted from a bending

simulation with known boundary conditions. The simulation is similar to the one from Figure 11 with different amplitudes (namely 1mm of imposed displacement). The displacement of the top surface is extracted and used to deformed the stereo images in order to create a (noise-free) artificial case using the camera calibration parameters of the real experiment described earlier.

The measured or extracted fluxes can thus be compared with the simulated ones to verify their validity. From the pair of artificial images, 4 additional sets of 10 noisy images were created and processed to extract moment fluxes using our regularized and the "Post-processed DIC" procedures. The noise level ranges from 0% to 25% of the dynamic range of the image. A classical Gaussian white noise model was used in this case.

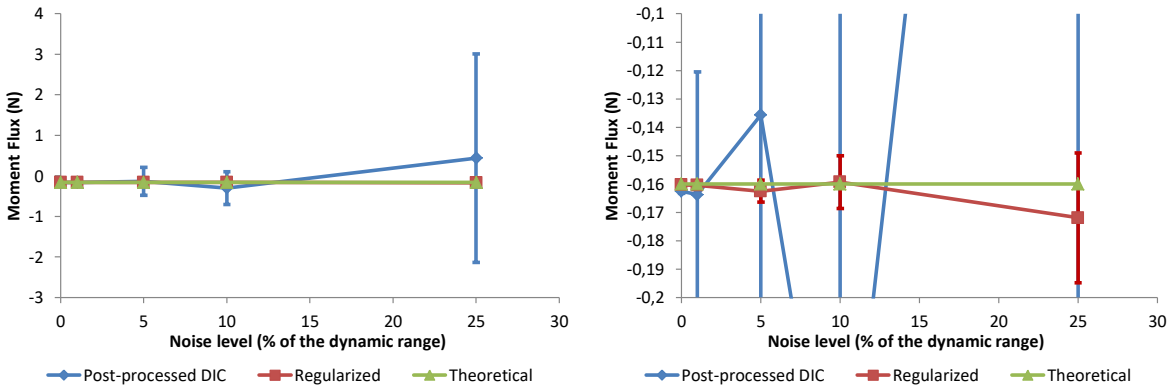

Figure 12 : Mean value of the moment flux estimation for each set of artificial images polluted by noise (left) ; Zoom around the theoretical level (right).

The expected value is -0.16 N which is the flux value of the simulation used to generate the artificial images. The fluxes were extracted using both methods for each set of data and the mean value and the standard deviation of the 10 results were computed. Figure 12 gathers the resulting flux estimation for these artificial cases. We can clearly see that the post-processed approach is significantly more impacted by the addition of noise than our regularized method which is not surprising given the filtering performed of the strong regularization. Moreover, even for small values of noise, the deviation of the measurement is significantly reduced using the strongly regularized DIC method. The analysis of this linear elastic sample problem validates the use of the strong regularization based procedure to extract fluxes. It shows the robustness to noise of the proposed technique as it provides a clear improvement in terms of uncertainties when compared to the former method relying on a posteriori displacement differentiations.

2.2. VERTEX tests

2.2.1. Test rig description

The experimental test rig used in this work is called "VERTEX test rig". It was developed by Castanié and first used by Serra et al. at the Institut Clément Ader in 2014 [6], [7]. The VERTEX test rig is based on the experience of a first similar test rig developed by Castanié et al. [54] that was used to test asymmetric sandwich structures implemented in helicopter fuselages. The test rig is made with one longitudinal box and four actuators to load the specimen, under membrane (shear and compression/tension) loading or internal pressure (Figure 13). The VERTEX specimen was bolted to the

upper surface of the center box structure with 128 fasteners. Once bolted to the test rig, the specimen area of interest was 400x400 mm^2 (Figure 14). The test rig was controlled with 4 actuators driven in displacement (Figure 13). When actuators 1 and 2 applied a vertical load, the structure was subjected to bending and the specimen forming the upper face of the center box was loaded in pure compression or pure tension. When only actuators 3 and 4 were activated, the center box was subjected to torsion and the plate was loaded in shear as illustrated on Figure 13 and Figure 14.

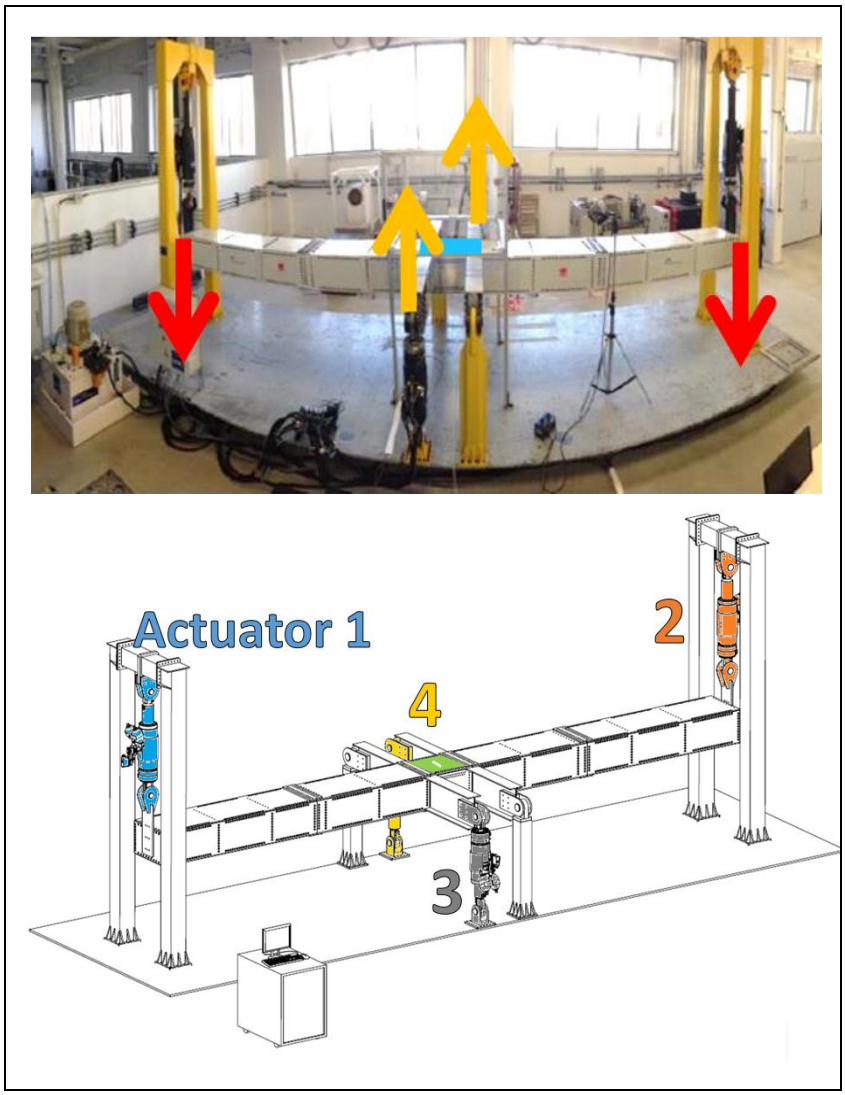

Figure 13: Deformed photography of the VERTEX test rig and the schematic diagram associated. Actuators move along the arrow directions.

As underlined by Serra et al. [16–18], a difficulty of this testing method is to have an accurate measurement of the value of the forces and moments fluxes entering the specimen during the test. Because of numerous structural redundancies (hyperstatism) of the test rig and the dependency of the test rig stiffness to the stiffness of the tested specimen, it is not easy to know the transfer function that links actuator forces to fluxes actually entering the specimen. To perform DIC, a speckled pattern was made on the whole specimen (Figure 14) and two 5 Mpx cameras recorded images from the whole specimen. The acquisition frequency was set to one frame per second.

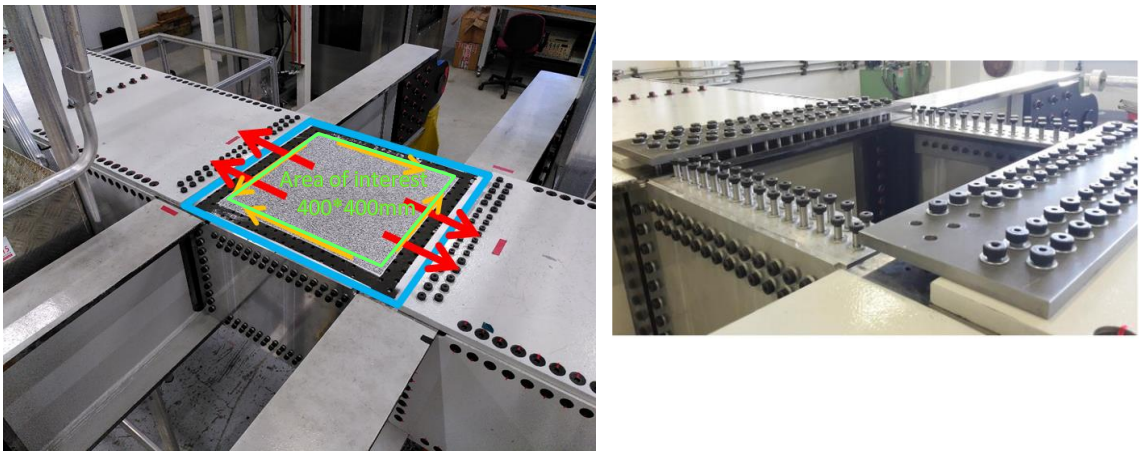

Figure 14: Area of interest and bolted junctions [6].
Arrows indicates the load applied by moving the corresponding actuators.

2.2.2. Shear test

In this paper, we chose to study a shear test performed on the VERTEX machine. The plate was made of 13 plies of T700/M21 carbon/epoxy prepeg. Each ply is 0.25mm thick and makes the total thickness of the specimen 3.25mm. The laminate orientations cannot be disclosed for confidentiality reasons. Each ply is considered quasi-isotropic transverse and the 5 material parameters used in the stiffness calculation are given in Table 1. Given the configuration of the test, the sample is expected to buckle along the diagonal between the top left and the bottom right corner of the plate.

E_l	115000 MPa
E_t	7700 MPa
G_{lt}	4750 MPa
ν_{lt}	0.25
ν_{tz}	0.38

Table 1 : Material parameters of the composite plies of the specimen

The out- of-plane displacement field obtained with DIC using a classical surface measurement is shown on Figure 15 (middle). The shear strain can also be visualized clearly on the X direction displacement field shown on Figure 16 (left). The strongly regularized DIC measurement method described previously was used to process the images, using a differentiated weight for the weak Tikhonov regularization of the edges along each direction as mentioned in section 2.1. Even though the test was performed up to failure, the results presented herein were selected before any significant (identifiable with thermal imaging) damage occurred.

The center part of the sample has also been removed from the analysis to avoid most of the inelastic effects (damage, fracture) occurring around the cut. The analysis is thus conducted in the elastic domain as far as the material is concerned.

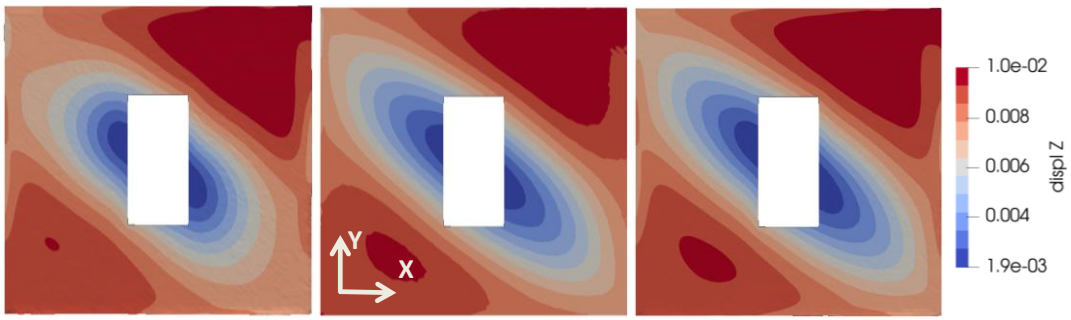

Figure 15 : Displacement field along the out of plane direction with linear regularization (left), and with non-linear regularization (right). These field can be compared to the global Stereo-DIC displacement field obtained (middle). The image is taken just before the first failure of the plate.

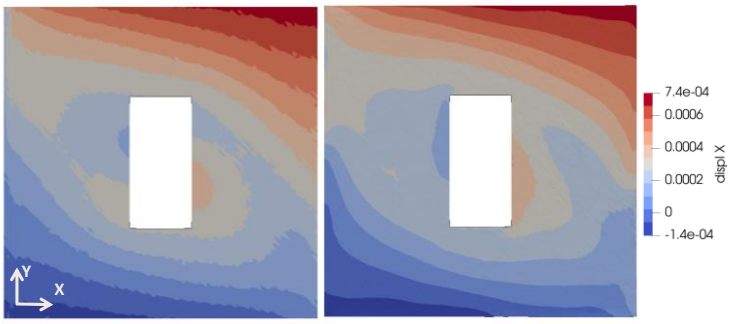

Figure 16: Displacement field along the X direction measured using a global Stereo-DIC (left) and a strongly regularized (right) DIC algorithm. The image is taken just before the first failure of the plate.

Figure 15 (left) shows the out-of-plane displacement field obtained using the strongly regularized DIC algorithm. The results are clearly different from the expected result shown on Figure 15 (center). We can see that the buckling effect is partly measured but the shape of the displacement field is not correct, as if the basis used to perform the measurement was not rich enough and the DIC could not capture completely the displacement of the buckle. Even though the material behavior is elastic, the buckling effect quickly becomes so important during the test that geometric non-linearity effects arise from the change in geometry. The global stiffness of the plate thus changes in a significant way which impacts the DIC process. Since this stiffness is used to create the basis function used in the algorithm (strong regularization), the resulting field is not accurate. One way to circumvent this effect is to re-compute the stiffness of the sample at each new image, in the spirit of a updated Lagrangian formulation of mechanically regularized DIC. This stiffness update thus creates a new accurate basis set that can be used to perform DIC. As such, this approach can be considered a (geometric) non-linear regularization to the DIC method, even if the material remains (linear) elastic in the region of interest. We will thus refer to the non-updated version of the regularized DIC as 'linear regularization' and to the updated version as 'non-linear regularization'. In practice, by passing the current configuration to the FE analysis software (Abaqus™ in our case) the stiffness is recomputed and used to create a new basis.

The new displacement obtained using the non-linear regularization is illustrated on Figure 15 (right) for the out-of-plane displacement and Figure 16 (right) for the X direction. The resulting displacements on the surface are much closer to the expected ones. This clearly demonstrates the importance of having proper stiffness estimation in this case. Given the specifics of the experiments performed using the VERTEX testing machine, the geometric non-linearity is an inherent part of most of the test cases

as most of the time, the loading will induce buckling. Our DIC method has thus been modified to update the stiffness of the model at every step.

Another way to account for the importance of updating the stiffness operator is to look at the residual map. Indeed, as mentioned above, a strong regularization implies that the measured field is strictly compatible with the regularization. If the regularization is inappropriate (as in the linear case), the solution is wrong and it results in abnormally high residuals. The correlation residuals in the linear elastic and the geometric non-linear elastic cases are shown in Figure 17. It can be seen, that the non-linear elastic regularization greatly improves the results, while the boundaries were not captured accurately with the linear elastic regularization.

Figure 17 : Zoom on the bottom right corner of the residual map $(I_{ref} - I_{def}(u))$ in pixels at convergence of the DIC process post-buckling (left) without and (right) with geometrically non-linear elastic regularization. The improvement is clearly visible on the edge of the plate.

It should be noted that computing a new basis L after processing an image does not guarantee the use of the proper stiffness for the following step, as this mainly depends on the acquisition frequency and the experiment speed. One way to account for this effect would consist in performing the DIC process and stiffness updating several times on the same image to ensure converge of both displacements and stiffness. Such an approach revealed unnecessary in this study.

In addition to the displacement field on the top surface, which is visible, the proposed strongly regularized DIC procedure provides additionally an estimate of the displacement field on bottom surface. Due to the mounting of the specimen in a box, it was not possible to compare this estimate to a conventional DIC measurement. In order to verify the validity of the measurement on the bottom surface of the specimen, we chose to check it against a few strain gauges placed on the non-visible side of the sample. Figure 18 illustrates the position of the strain gauges on the real sample and on the virtual model used for this comparison. Each gauge is positioned mid distance between the cut and the boundary of the sample, as described on Figure 18 (center).

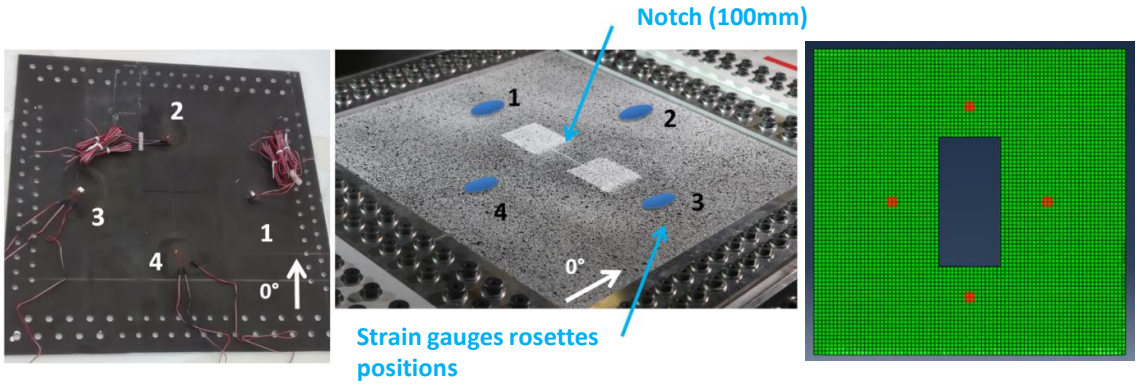

Figure 18: (Left and center) Gauges position on the real sample; (right) virtual gauges used on the FE model.

The comparison between the experimental strain gauges and the virtual ones on the bottom part of the specimen is presented in Figure 19. During this experiment, the gauges (solid lines) are registering mainly shear deformations, as expected. Several plateaus were performed in order to take pictures and can be clearly distinguished on the data. The strains extracted from the FE simulation corresponding to the DIC (symbols) are consistent with the data in the experiment especially regarding the shear, which is the main solicitation in the sample during the test.

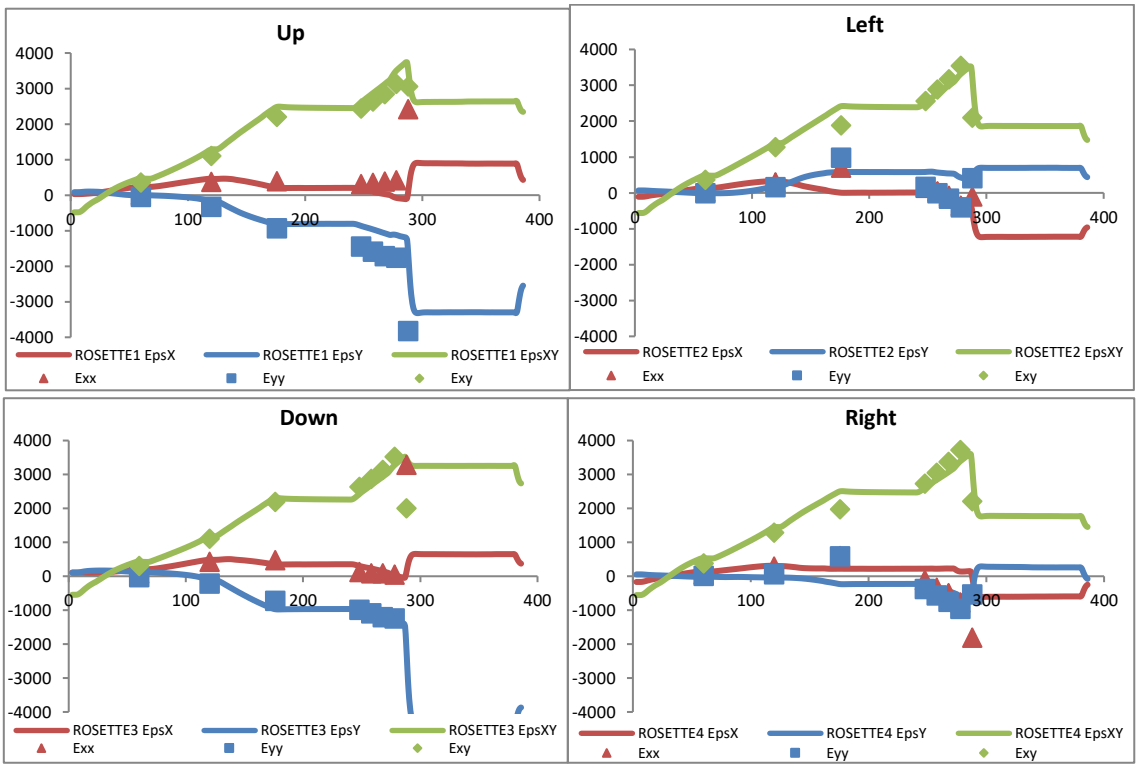

Figure 19: Comparison between strain values on the hidden face of the plate obtained with gauges (solid lines) and extracted from the I-FE-SDIC measurement (symbols)

We can observe that critical damage occurs around 280s after the beginning of the test, creating a sudden drop in the measured strains. The painted pattern used on the specimen is fragmented and projected towards the cameras at this point, thus creating artifacts on the images. The behavior is clearly non-linear and not considered in the mechanical regularization (as the stiffness calculation is

performed using an elastic model with no damage) but the method is still capable to capture it for the right and left virtual gauges. As the crack is propagating from the tip of the notch, top and bottom gauges are experiencing more pronounced non-linear effects, whereas the left and right zones are significantly less impacted. This can be considered a clear validation of the measurement even on the non-visible face of the sample, and clearly indicates that the boundary conditions extracted from our DIC algorithm can be used with confidence.

Forces and moments fluxes can be extracted from the simulation associated with our DIC measurement method or by post-processing the classic subset DIC results. A summary of the loading fluxes for each the time step processed is presented on Figure 20. The load is mainly shear, with a component of compression along the X direction. The extracted values are consistent with the expected results.

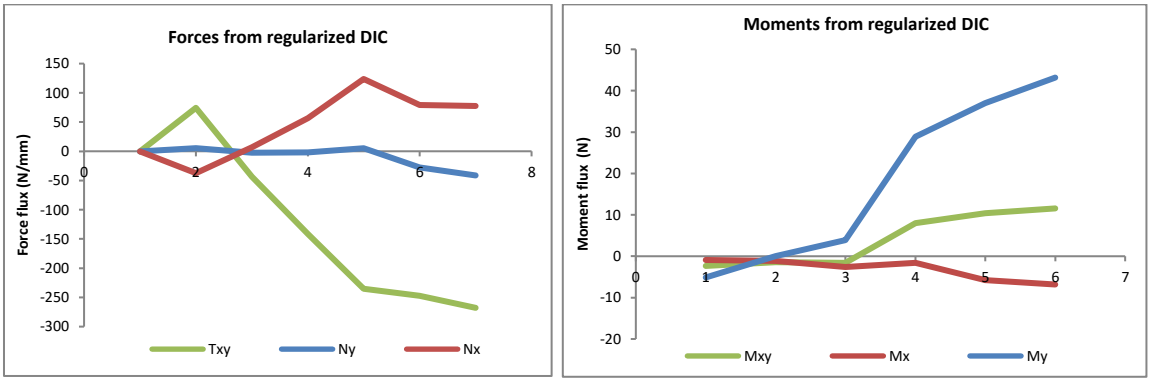

Figure 20 : Fluxes extracted from the regularized DIC

3. Conclusion

In this paper, the concept of strong regularization was extended to geometric non-linearities and the use of I-FESDIC starting was demonstrated with a simple bending plate configuration. It was shown that noise can lead to erroneous estimations of forces and moments fluxes. The impact of a penalization coefficient on the Tikhonov regularization was investigated and it came that not only it should be picked large enough to avoid singular matrix issues and low enough to avoid non-physical solutions. Outside of these extreme values, this parameter proved to be quite insensitive. Conversely, it has been shown that choosing it differently depending on the direction is of the utmost importance.

The study of the post-buckling behavior of a composite plate tested on the VERTEX rig also illustrated the necessity of re-computing the stiffness operator at each processed image in order to account for the geometric non-linearities of the model. It is only in this way that it was possible to perform correct measurements on both the upper layer and the bottom layer thanks to the strong regularization of the DIC algorithm.

The proposed approach was validated by comparing the corresponding measurement results to strain gauges applied on the hidden face of the specimen. The method managed to accurately capture the deformation using only the opposite face images and assumptions on the material behavior of the plate.

This new formulation therefore makes it possible to access both regularized fluxes without extra steps that would decrease the quality of its quantification and accurate boundary conditions on a single prismatic surface through the knowledge of both upper and lower surface displacement.

Funding

This work has been funded by the "Fondation Jean-Jacques et Felicia Lopez-Loreta pour l'Excellence Académique" as part of the VIRTUOSE (**VIRTU**al testing of aer**O**nautical **S**tructur**E**s) project (https://websites.isae-supaero.fr/virtuose/).
This work was granted access to the HPC resources of CALMIP under allocation 2021-P21002

Competing interest

The authors have no competing interests to declare that are relevant to the content of this article.

References

[1] D. Gay, S. V. Hoa, and S. W. Tsai, *Composite Materials: Design and Applications*. Boca Raton: CRC Press, 2002. doi: 10.1201/9781420031683.
[2] J. Rouchon, 'Certification of Large Airplane Composite Structures, Recent Progress and New Trends in Compliance Philosophy', presented at the ICAS, 1990. Accessed: Jan. 11, 2022. [Online]. Available: https://www.icas.org/ICAS_ARCHIVE/ICAS1990/ICAS-90-1.8.1.pdf
[3] T. Bru, 'Material characterisation for crash modelling of composites [PhD thesis]', 2018. doi: 10.13140/RG.2.2.10536.01280.
[4] F. Grotto, J. Serra, C. Bouvet, and B. Castanié, 'Structural testing of large notched composite specimens under combined shear and pressure', Porto, Portugal, Jun. 2021. Accessed: Jan. 12, 2022. [Online]. Available: https://hal.archives-ouvertes.fr/hal-03407636
[5] Joint Airworthiness Requirements 25 (JAR25), 'Part 1: requirements, Part 2: acceptable means of compliance and interpretations'. (for composite structures: JAR25 § 25.603 and ACJ 25.603), 1978.
[6] J. Serra, J. E. Pierré, J. C. Passieux, J. N. Périé, C. Bouvet, and B. Castanié, 'Validation and modeling of aeronautical composite structures subjected to combined loadings: The VERTEX project. Part 1: Experimental setup, FE-DIC instrumentation and procedures', *Compos. Struct.*, vol. 179, pp. 224–244, Nov. 2017, doi: 10.1016/j.compstruct.2017.07.080.
[7] J. Serra, J. E. Pierré, J. C. Passieux, J. N. Périé, C. Bouvet, B. Castanié and C. Petiot, 'Validation and modeling of aeronautical composite structures subjected to combined loadings: The VERTEX project. Part 2: Load envelopes for the assessment of panels with large notches', *Compos. Struct.*, vol. 180, pp. 550–567, Nov. 2017, doi: 10.1016/j.compstruct.2017.08.055.
[8] E. Abisset, F. Daghia, and P. Ladevèze, 'On the validation of a damage mesomodel for laminated composites by means of open-hole tensile tests on quasi-isotropic laminates', *Compos. Part Appl. Sci. Manuf.*, vol. 42, no. 10, pp. 1515–1524, Oct. 2011, doi: 10.1016/j.compositesa.2011.07.004.
[9] L. Marcin, J.-F. Maire, N. Carrère, E. Martin 'Development of a Macroscopic Damage Model for Woven Ceramic Matrix Composites', *Int. J. Damage Mech.*, vol. 20(6), pp. 939-957, 2011. doi:10.1177/1056789510385259
[10] F. Laurin, N. Carrere, C. Huchette, and J.-F. Maire, 'A multiscale hybrid approach for damage and final failure predictions of composite structures', *J. Compos. Mater.*, vol. 47, no. 20–21, pp. 2713–2747, Sep. 2013, doi: 10.1177/0021998312470151.

[11] P. P. Camanho, G. H. Erçin, G. Catalanotti, S. Mahdi, and P. Linde, 'A finite fracture mechanics model for the prediction of the open-hole strength of composite laminates', *Compos. Part Appl. Sci. Manuf.*, vol. 43, no. 8, pp. 1219–1225, Aug. 2012, doi: 10.1016/j.compositesa.2012.03.004.
[12] J.-F. Chen, E. V. Morozov, and K. Shankar, 'Simulating progressive failure of composite laminates including in-ply and delamination damage effects', *Compos. Part Appl. Sci. Manuf.*, vol. 61, pp. 185–200, Jun. 2014, doi: 10.1016/j.compositesa.2014.02.013.
[13] J. Serra, C. Bouvet, B. Castanié, and C. Petiot, 'Scaling effect in notched composites: The Discrete Ply Model approach', *Compos. Struct.*, vol. 148, pp. 127–143, Jul. 2016, doi: 10.1016/j.compstruct.2016.03.062.
[14] J. Serra, C. Bouvet, B. Castanié, and C. Petiot, 'Experimental and numerical analysis of Carbon Fiber Reinforced Polymer notched coupons under tensile loading', *Compos. Struct.*, vol. 181, pp. 145–157, Dec. 2017, doi: 10.1016/j.compstruct.2017.08.090.
[15] T. Laux, K. Wui Gan, R. P. Tavares, C. Furtado, A. Arteiro, P. P. Camanho, O. T Thomsen, J. M. Dulieu-Barton, 'Modelling damage in multidirectional laminates subjected to multi-axial loading: Ply thickness effects and model assessment', *Compos. Struct.*, Mar. 2021, doi: 10.1016/j.compstruct.2021.113766.
[16] A. Trellu, G. Pichon, C. Bouvet, S. Rivallant, B. Castanié, J. Serra, L. Ratsifandrihana, 'Combined loadings after medium velocity impact on large CFRP laminate plates: Tests and enhanced computation/testing dialogue', *Compos. Sci. Technol.*, vol. 196, p. 108194, Aug. 2020, doi: 10.1016/j.compscitech.2020.108194.
[17] J. Serra, A. Trellu, C. Bouvet, S. Rivallant, B. Castanié, and L. Ratsifandrihana, 'Combined loadings after medium velocity impact on large CFRP laminated plates: Discrete ply model simulations', *Compos. Part C Open Access*, vol. 6, p. 100203, Oct. 2021, doi: 10.1016/j.jcomc.2021.100203.
[18] N. A. Kallemeyn, N. M. Grosland, D. R. Pedersen, J. A. Martin, and T. D. Brown, 'Loading and boundary condition influences in a poroelastic finite element model of cartilage stresses in a triaxial compression bioreactor', *Iowa Orthop. J.*, vol. 26, pp. 5–16, 2006.
[19] R. E. Darlington and T. C. Becker, 'Stiffness of Rubber Bearings Considering Nonstandard Top and Bottom Boundary Conditions', *J. Struct. Eng.*, vol. 147, no. 7, p. 04021101, Jul. 2021, doi: 10.1061/(ASCE)ST.1943-541X.0003052.
[20] H. Rostami, A. Osouli, B. Vaughn, and H. Gholizadeh Touchaei, 'Influence of Boundary Conditions on Response of Pipelines Crossing Reverse Fault Zone', pp. 180–189, Nov. 2021, doi: 10.1061/9780784483701.018.
[21] R. Fedele, B. Raka, F. Hild, and S. Roux, 'Identification of adhesive properties in GLARE assemblies using Digital Image Correlation', *J. Mech. Phys. Solids*, vol. 57, pp. 1003–1016, 2009.
[22] A. Carpiuc-Prisacari, M. Poncelet, K. Kazymyrenko, F. Hild, and H. Leclerc, 'Comparison between experimental and numerical results of mixed-mode crack propagation in concrete: Influence of boundary conditions choice', *Cem. Concr. Res.*, vol. 100, pp. 329–340, Oct. 2017, doi: 10.1016/j.cemconres.2017.05.003.
[23] J.-S. Affagard, F. Mathieu, J.-M. Guimard, and F. Hild, 'Identification method for the mixed mode interlaminar behavior of a thermoset composite using displacement field measurements and load data', *Compos. Part Appl. Sci. Manuf.*, vol. 91, pp. 238–249, Dec. 2016, doi: 10.1016/j.compositesa.2016.10.007.
[24] J.-E. Dufour, F. Hild, and S. Roux, 'Shape, displacement and mechanical properties from isogeometric multiview stereocorrelation', *J. Strain Anal. Eng. Des.*, vol. 50, no. 7, pp. 470–487, Oct. 2015, doi: 10.1177/0309324715592530.
[25] T. Elguedj, J. Réthoré, and A. Buteri, 'Isogeometric analysis for strain field measurements', *Comput. Methods Appl. Mech. Eng.*, vol. 200, no. 1, pp. 40–56, Jan. 2011, doi: 10.1016/j.cma.2010.07.012.
[26] J. Réthoré, T. Elguedj, P. Simon, and M. Coret, 'On the Use of NURBS Functions for Displacement Derivatives Measurement by Digital Image Correlation', *Exp. Mech.*, vol. 50, no. 7, pp. 1099–1116, Sep. 2010, doi: 10.1007/s11340-009-9304-z.

[27] Y. Sun, J. H. L. Pang, C. K. Wong, and F. Su, 'Finite element formulation for a digital image correlation method', *Appl. Opt.*, vol. 44, no. 34, p. 7357, Dec. 2005, doi: 10.1364/AO.44.007357.
[28] J.-E. Pierré, J.-C. Passieux, and J.-N. Périé, 'Finite Element Stereo Digital Image Correlation: Framework and Mechanical Regularization', *Exp. Mech.*, vol. 57, no. 3, pp. 443–456, Mar. 2017, doi: 10.1007/s11340-016-0246-y.
[29] F. Hild and S. Roux, 'Comparison of local and global approaches to digital image correlation', *Exp. Mech.*, vol. 52, no. 9, pp. 1503–1519, 2012, doi: 10.1007/s11340-012-9603-7.
[30] P. Sztefek and R. Olsson, 'Non-linear compressive stiffness in impacted composite laminates determined by an inverse method', *Compos. Part Appl. Sci. Manuf.*, vol. 40, no. 3, pp. 260–272, Mar. 2009, doi: 10.1016/j.compositesa.2008.12.002.
[31] A. Carpiuc, M. Poncelet, J. Réthoré, and S. Roux, 'CARPIUC benchmark overview: crack advance, reorientation, propagation and initiation under complex loadings', *Adv. Model. Simul. Eng. Sci.*, vol. 5, no. 1, Dec. 2018, doi: 10.1186/s40323-018-0115-6.
[32] R. Fedele, 'Simultaneous Assessment of Mechanical Properties and Boundary Conditions Based on Digital Image Correlation', *Exp. Mech.*, vol. 55, Aug. 2014, doi: 10.1007/s11340-014-9931-x.
[33] F. Mathieu, P. Aimedieu, J.-M. Guimard, and F. Hild, 'Identification of interlaminar fracture properties of a composite laminate using local full-field kinematic measurements and finite element simulations', *Compos. Part Appl. Sci. Manuf.*, vol. 49, pp. 203–213, Jun. 2013, doi: 10.1016/j.compositesa.2013.02.015.
[34] A. M. Peshave, D. Vandepitte, D. Moens, and P. Lava, 'Towards Identification of Spatial Uncertainties in Materials using Digital Image Correlation', presented at the International Digital Image Correlation Society Virtual Conference 2020, Nantes, France, 2021.
[35] Z. Tomičević, F. Hild, and S. Roux, 'Mechanics-aided digital image correlation', *J. Strain Anal. Eng. Des.*, vol. 48, no. 5, Art. no. 5, Jul. 2013, doi: 10.1177/0309324713482457.
[36] S. Roux and F. Hild, 'Stress intensity factor measurements from digital image correlation: post-processing and integrated approaches', *Int. J. Fract.*, vol. 140, no. 1, pp. 141–157, Jul. 2006, doi: 10.1007/s10704-006-6631-2.
[37] J. Gao and H. Shang, 'Deformation-pattern-based digital image correlation method and its application to residual stress measurement', *Appl. Opt.*, vol. 48, no. 7, p. 1371, Mar. 2009, doi: 10.1364/AO.48.001371.
[38] F. Hild, S. Roux, N. Guerrero, M. E. Marante, and J. Flórez-López, 'Calibration of constitutive models of steel beams subject to local buckling by using digital image correlation', *Eur. J. Mech. - ASolids*, vol. 30, no. 1, pp. 1–10, Jan. 2011, doi: 10.1016/j.euromechsol.2010.09.007.
[39] A. Baldi, 'Residual Stress Measurement Using Hole Drilling and Integrated Digital Image Correlation Techniques', *Exp. Mech.*, vol. 54, no. 3, pp. 379–391, Mar. 2014, doi: 10.1007/s11340-013-9814-6.
[40] J. Réthoré, F. Hild, and S. Roux, 'Extended digital image correlation with crack shape optimization', *Int. J. Numer. Methods Eng.*, vol. 73, no. 2, pp. 248–272, 2008, doi: 10.1002/nme.2070.
[41] A. Mendoza, J. Neggers, F. Hild, and S. Roux, 'Complete mechanical regularization applied to digital image and volume correlation', *Comput. Methods Appl. Mech. Eng.*, vol. 355, pp. 27–43, Oct. 2019, doi: 10.1016/j.cma.2019.06.005.
[42] J. Neggers, J. P. M. Hoefnagels, M. G. D. Geers, F. Hild, and S. Roux, 'Time-resolved integrated digital image correlation: TIME-RESOLVED INTEGRATED DIGITAL IMAGE CORRELATION', *Int. J. Numer. Methods Eng.*, vol. 103, no. 3, Art. no. 3, Jul. 2015, doi: 10.1002/nme.4882.
[43] A. Rouwane, R. Bouclier, J.-C. Passieux, and J.-N. Périé, 'Architecture-Driven Digital Image Correlation Technique (ADDICT) for the measurement of sub-cellular kinematic fields in speckle-free cellular materials', *Int. J. Solids Struct.*, vol. 234–235, p. 111223, Jan. 2022, doi: 10.1016/j.ijsolstr.2021.111223.
[44] J. P. M. Hoefnagels, K. van Dam, N. Vonk, and L. Jacobs, 'Accurate Strain Field Measurement During Strip Rolling by Exploiting Recurring Material Motion with Time-Integrated Digital Image Correlation', *Exp. Mech.*, Dec. 2021, doi: 10.1007/s11340-021-00781-y.

[45] J. Réthoré, Muhibullah, T. Elguedj, M. Coret, P. Chaudet, and A. Combescure, 'Robust identification of elasto-plastic constitutive law parameters from digital images using 3D kinematics', *Int. J. Solids Struct.*, vol. 50, no. 1, pp. 73–85, Jan. 2013, doi: 10.1016/j.ijsolstr.2012.09.002.
[46] J. Réthoré, 'A fully integrated noise robust strategy for the identification of constitutive laws from digital images', *Int. J. Numer. Methods Eng.*, vol. 84, no. 6, pp. 631–660, Nov. 2010, doi: 10.1002/nme.2908.
[47] J. Réthoré, S. Roux, and F. Hild, 'An extended and integrated digital image correlation technique applied to the analysis of fractured samples: The equilibrium gap method as a mechanical filter', *Eur. J. Comput. Mech.*, vol. 18, no. 3–4, pp. 285–306, Jan. 2009, doi: 10.3166/ejcm.18.285-306.
[48] H. Leclerc, J.-N. Périé, S. Roux, and F. Hild, 'Integrated Digital Image Correlation for the Identification of Mechanical Properties', in *Computer Vision/Computer Graphics CollaborationTechniques*, vol. 5496, A. Gagalowicz and W. Philips, Eds. Berlin, Heidelberg: Springer Berlin Heidelberg, 2009, pp. 161–171. doi: 10.1007/978-3-642-01811-4_15.
[49] S. Roux, F. Hild, and H. Leclerc, 'Mechanical Assistance to DIC', *Procedia IUTAM*, vol. 4, pp. 159–168, 2012, doi: 10.1016/j.piutam.2012.05.018.
[50] A. Charbal, J.-E. Dufour, A. Guery, F. Hild, S. Roux, L. Vincent, M. Poncelet, 'Integrated Digital Image Correlation considering gray level and blur variations: Application to distortion measurements of IR camera', *Opt. Lasers Eng.*, vol. 78, pp. 75–85, Mar. 2016, doi: 10.1016/j.optlaseng.2015.09.011.
[51] J.-E. Dufour, F. Hild, and S. Roux, 'Integrated digital image correlation for the evaluation and correction of optical distortions', *Opt. Lasers Eng.*, vol. 56, pp. 121–133, May 2014, doi: 10.1016/j.optlaseng.2013.12.015.
[52] A. Baldi and F. Bertolino, 'Integrated digital image correlation for residual stress measurement', in *Optical Measurement Systems for Industrial Inspection VIII*, May 2013, vol. 8788, pp. 558–563. doi: 10.1117/12.2020758.
[53] R. Balcaen, L. Wittevrongel, P. L. Reu, P. Lava, and D. Debruyne, 'Stereo-DIC Calibration and Speckle Image Generator Based on FE Formulations', *Exp. Mech.*, vol. 57, no. 5, pp. 703–718, Feb. 2017, doi: 10.1007/s11340-017-0259-1.
[54] B. Castanie, 'Combined Shear/Compression Structural Testing of Asymmetric Sandwich Structures', *Exp. Mech.*, vol. 44, no. 5, pp. 461–472, Oct. 2004, doi: 10.1177/0014485104047607.